Bridging the Gap: Electrode Microstructure and Interphase Characterization by Combining ToF-SIMS and Machine Learning

Teo Lombardo, Christine Kern, Joachim Sann, Marcus Rohnke, and Jürgen Janek**

This article presents a new analytical methodology to analyze large (hundreds of µm) battery electrode microstructures by mapping the spatial distribution of the main phases (e.g., active material and carbon-binder domain) and degradation products (solid- or cathode-electrolyte interphase) formed during cycling. The methodology can be used for a better understanding of the relationships between electrode architecture and degradation, paving the way toward the analysis of interphases spatial distribution and their correlations to the electrode formulation, microstructure, and cycling conditions. This work is based on time-of-flight secondary ion mass spectrometry (ToF-SIMS), and focuses on analyzing large 2D electrode cross-sections at both the microstructure and single particle/agglomerate level. It also shows that this analysis can be expanded to 3D electrode microstructures when combining ToF-SIMS and devoted machine learning procedures, which can be of particular interest to the 3D electrochemical modeling community.

1. Introduction

Li-ion and post-Li-ion battery electrodes are complex composite materials whose key properties, like specific capacity, cycle life, and safety, are not only dictated by the materials used and their weight fractions (i.e., the electrode formulation), but also by their spatial distribution and interfaces (i.e., the electrode microstructure). The role of the electrode microstructure is vastly recognized in the literature, and many studies focus on linking electrode microstructure and electrochemical performance on the one hand, and electrode microstructure and manufacturing processes on the other hand.[1–16]

3D electrode microstructure characterization, mainly based on focused-ion beam secondary electron microscopy (FIB-SEM) or X-ray tomography, has significantly improved over the past decades. While FIB-SEM utilization for investigating large fractions of 3D electrode microstructure (tens of µm per direction) is increasingly common in battery research,[17–19] X-ray tomography applied to cathodes often falls short in identifying the spatial distribution of conductive and binder additives (carbon binder domain – CBD). This is caused by their lower atomic weight compared to the active material (AM), which is typically composed of transition metal oxides.[20,21] This limitation led to a number of computational approaches, like the binder–bridge approach,[22–24] to model realistic carbon and binder spatial distribution using the identified AM matrix as a starting point. These approaches, however, seem to be already outdated, considering recent advances allowing the identification of both AM and CBD spatial distributions.[25,26]

In addition to the electrode formulation and microstructure, interfaces and interphases, i.e., cathode and solid-electrolyte interphases (CEI and SEI, respectively) or mixed conducting interphases (MCI), play a critical role.[27] Therefore, it would be of particular interest being capable of analyzing the electrode microstructure together with the spatial distribution and chemical composition of interphases. However, to date neither FIB-SEM nor X-ray tomography can identify the spatial location of SEI, CEI, or MCI due to their nanometric size and low contrast. This work aims to introduce a new analytical methodology, based on time-of-flight secondary ion mass spectrometry (ToF-SIMS), enabling the identification and characterization of the spatial distribution of the electrode main components and interphases, representing a step forward in electrode microstructure characterization.

ToF-SIMS uses an ion gun that produces a focused (primary) ion beam that hits the sample, ablating and fragmenting the chemical species originally present at its surface. The so-formed fragments can get ionized through a cascade process (as a function of their ionization probability) forming so-called secondary

T. Lombardo, C. Kern, J. Sann, M. Rohnke, J. Janek
Institute of Physical Chemistry & Center for Materials Research (ZfM/LaMa)
Justus Liebig University Giessen
35392 Giessen, Germany
E-mail: Marcus.Rohnke@phys.chemie.uni-giessen.de;
Juergen.Janek@phys.chemie.uni-giessen.de

The ORCID identification number(s) for the author(s) of this article can be found under https://doi.org/10.1002/admi.202300640

© 2023 The Authors. Advanced Materials Interfaces published by Wiley-VCH GmbH. This is an open access article under the terms of the Creative Commons Attribution License, which permits use, distribution and reproduction in any medium, provided the original work is properly cited.

DOI: 10.1002/admi.202300640

ions (SIs), which are then collected by an extraction field and analyzed in the time-of-flight analyzer in terms of their mass over charge (m/z) ratio. This data can then be used to identify the chemical species originally present at the sample surface. In addition, ToF-SIMS has a high sensitivity (down to <10 ppm) and can reach high lateral resolution (<50 nm) and field of view (up to a few hundred μm). Despite these characteristics, ToF-SIMS is still rarely utilized in battery research and there is significant unexplored potential for future research.

In the context of this work, ToF-SIMS was used to map the spatial distribution of the main phases and interphases present on cycled electrode cross-sections (2D microstructure). SIMS-based image segmentation was performed by applying an in-house python code. Identification and characterization of single particles/agglomerates was performed through a watershed-based algorithm. The segmented images were also used to train a machine learning (ML) algorithm, SliceGAN, recently published by Kench et al.[28] and allowing to reconstruct statistically representative 3D microstructures using 2D microstructures as input. This approach has largely been tested,[29] and it is applied here for the first time to SI-based images. The combination of ToF-SIMS and SliceGAN unlocks the reconstruction of realistic 3D microstructures containing not only information on the spatial distribution of active material and additives, but also on the spatial location of the interphases.

The results chapter is divided into three parts. Section 2.1 discusses the ToF-SIMS methodology developed in this work and presents the first results obtained for state-of-the-art lithium-ion battery (LIB) electrodes, in particular graphite-silicon anodes and a $LiNi_{0.6}Mn_{0.2}Co_{0.2}O_2$ (NMC) cathode. Section 2.2 lists the current drawbacks and limitations of our approach and good practices that should be followed. Section 2.3 discusses the combination of SIMS-based 2D microstructure imaging and SliceGAN to obtain statistically representative 3D electrode microstructures. Lastly, the conclusions summarize the work discussed in this article and present the main perspectives we can foresee.

2. Results and Discussion

2.1. Methodology and Proof of Concept

The electrode to be analyzed by ToF-SIMS is positioned within a sample holder that exposes the electrode cross-section to the SIMS analyzer (Figure S1, Supporting Information), which is first polished with a FIB gun, followed by the utilization of the primary ion gun in direct current (DC) mode for surface cleaning. Afterward, the cross-section is analyzed in delayed extraction (DE) mode, which is a measurement mode that allows combining high lateral resolution (i.e., well-resolved images) and high mass resolution to better distinguish different SIs with similar masses. In short, DE mode combines the advantages of high mass resolution and high lateral resolution imaging modes at the cost of longer measurement time.[30] DE decouples the mass resolution from the length of the primary ion pulse by applying the voltage used to accelerate and collect the SIs into the ToF analyzer after a certain time delay. This leads to an improved mass resolution combined with high lateral resolution. The main disadvantages of the DE mode are that lower masses (typically <30 m/z) are lost during the delay time and that the SI yield is reduced, increasing the measurement time from a few minutes (low lateral resolution, high mass resolution) or ca. 1 h (high lateral resolution, low mass resolution) to several hours. The samples were found to be stable under the used measurement conditions despite the long measurement times (Figure S7, Supporting Information).

In the ToF-SIMS measurements presented here, the analyzed field of view was of 250 × electrode thickness μm² for all images and we reached a pixel resolution of ca. 125 nm. All ToF-SIMS analyses were performed in negative ion mode because typical degradation products, such as phosphates, carbonates, and hydroxides, tend to form negatively charged fragments. A full SI mass spectrum is measured for each pixel of the region of analysis, and the total secondary ion intensity (the area underneath all the peaks for each spectrum/pixel) can be displayed to visualize the overall electrode microstructure (**Figure 1**A). This approach, however, does not allow distinguishing between the different phases. Contrary, a single (or a combination of) peak(s) can be used to display the associated SI image. If the SI is specific for a certain electrode phase, this image shows the spatial distribution of that phase (Figure 1B). Finally, these phase-specific SI images can be overlayed (Figure 1C) and segmented (i.e., each pixel is assigned to one phase only, here the one with the highest relative intensity). An example of SI-based image segmentation workflow is shown in Figure S2 (Supporting Information).

Once a segmented image is obtained, it is possible to analyze both the overall volume fraction of the different phases and their interfaces. More interestingly, single particles or particle agglomerates can be identified to analyze their size/shape distribution and interfaces. An example for the case of silicon agglomerates within an uncycled graphite-silicon anode can be found in **Figure 2**. The identification of single particles/agglomerates was carried out through a watershed-based procedure and the associated Python code is published together with this article.

In addition, thanks to the high-sensitivity of ToF-SIMS, also low concentration species can be detected, if their ionization probability is high enough. This allows, for example, mapping the degradation products that are expected to be part of the SEI and use them as a fingerprint for the SEI spatial distribution. The latter is also possible if the interphase thickness is below the lateral resolution limit. This information can then be added to the final segmented electrode microstructure (**Figure 3**A). Importantly, this methodology can be used to get a good approximation of the spatial distribution of the SEI, but it cannot be used to quantify its amount. Indeed, if the pixel resolution (100–150 nm) is bigger than the expected SEI thickness (up to a few tens nm), the identification of SEI-related species in a given pixel does not mean that the entirety of this region is filled with SEI, but most likely just a fraction of it. In addition, it should be reminded that ToF-SIMS is a semi-quantitative technique, which would also hamper a proper SEI quantification.

In the case of graphite-silicon anodes, the SEI spatial location was identified using LiO^- and $LiCO_2^-$ as reference SI because of their relatively high-intensity and because Li_2O, LiOH, and $LiCO_3$ are all compounds that are commonly found in the SEI.[31,32] When analyzing the uncycled (pristine) anode, no significant SI intensity was detected for both LiO^- and $LiCO_2^-$ (Figure S5, Supporting Information). This can be noted in Figure 3B, in which the percentage of each silicon agglomerate surface covered by graphite, SEI, or pore is reported for both

© 2023 The Authors. Advanced Materials Interfaces published by Wiley-VCH GmbH

21967350, 2023, 36, Downloaded from https://onlinelibrary.wiley.com/doi/10.1002/admi.202300640 by Justus Liebig Universitaet Giessen, Wiley Online Library on [02/10/2024]. See the Terms and Conditions (https://onlinelibrary.wiley.com/terms-and-conditions) on Wiley Online Library for rules of use; OA articles are governed by the applicable Creative Commons License

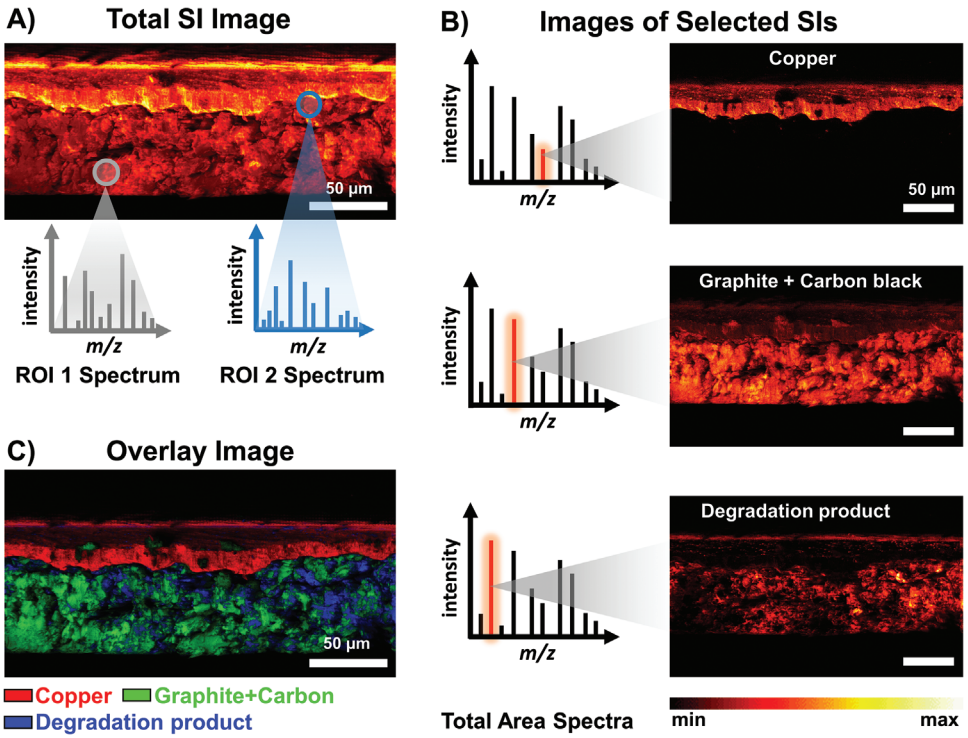

Figure 1. Schematic representation of a ToF-SIMS-based electrode cross-section analysis for the case of a calendered graphite composite anode. A) The total ion image shows the overall electrode microstructure. Mass spectra of individual regions of interest (ROIs) can be studied. B) SI images of different peaks from the total mass spectrum. C) Overlay image shows copper in red, graphite + carbon in green, and an example of a degradation product in blue. All scalebars represent 50 µm.

pristine (top) and lithiated (bottom) electrodes. As can be seen in Figure 3B, no significant SEI-associated signal is detected before cycling, while a significant particle coverage (in a wide range spanning between ≈ 0 and 80%) was found even after short cycling (30% lithiation) against lithium metal.

This procedure has also been tested for cycled NMC-based cathodes. On the one hand, this shows the flexibility of this approach that in principle can be adapted to any LIBs or post-LIB chemistry. On the other hand, this example is functional to illustrate an important risk associated with this approach, if the analysis is not carried out carefully. **Figure 4** shows the 2D microstructure of a cycled NMC electrode accounting for the NMC, CBD, and CEI phases. Figure 4A utilizes $LiCO_3^-$ and CO_3^- as the reference SI to map the CEI spatial distribution, while Figure 4B utilizes PO_3^- instead. Comparing these two images it can clearly be seen that the resulting CEI amount and its spatial distribution differ drastically, and that using PO_3^- as the reference SI leads to an unrealistically thick CEI. This underlines the importance of an appropriate choice of SI(s) to be used as a reference for interphases such as CEI, SEI, or MCI, and represents one of the main pitfalls of this methodology in its current form.

This difference is likely to originate from the fundamental operating principle of SIMS.

Before discussing this, it should be mentioned that the signal intensity for a given SI (Equation S1, Supporting Information) does not only depend on the species concentration on the sample surface, but also on the sputter yield (i.e., how many of those molecular fragments are sputtered due to the impact between the primary ions and the sample surface), the ionization probability (i.e., how many of the sputter fragments are ionized and can therefore be detected), and how many of the generated SI reach the analyzer.

ToF-SIMS is a surface-sensitive technique, but the electrode cross-section is not fully dense. There are indeed pores, and particles underneath them. However, it is often possible to approximate that the underneath particles are not being analyzed because of the lower flux of primary ions reaching them in unfavorable angles and because the associated SIs have a lower probability to reach the analyzer, as they might hit the particles overhead or not live long enough to reach it. Nonetheless, if the selected SI has both very high ionization probability and lifetime, this can lead to detecting the SI generated from the underneath particles. This is likely the case for PO_3^-, which led us to the hypothesis that the thick CEI identified using it as a reference signal (Figure 4B) is caused by SI coming from both overhead and underneath particles, and where the contribution of the latter is not negligible. This implies that the most appropriate reference SI for the specific case study should be carefully chosen.

In the case study carried out here, it was found that using the PO_3^- isotope $P^{18}OO_2^-$ as reference, SI allows getting rid of this artifact. This is due to the lower formation probability of $P^{18}OO_2^-$ compared to PO_3^-. Therefore, using the $P^{18}OO_2^-$ signal is similar to applying a threshold to the PO_3^- signal. In this way, only the signals originating from the surface can be used to map the CEI distribution and not the signals originating from deeper regions. Therefore, the best combination of SIs to identify the

© 2023 The Authors. Advanced Materials Interfaces published by Wiley-VCH GmbH

21967350, 2023, 36, Downloaded from https://onlinelibrary.wiley.com/doi/10.1002/admi.202300640 by Justus Liebig Universitaet Giessen, Wiley Online Library on [02/10/2024]. See the Terms and Conditions (https://onlinelibrary.wiley.com/terms-and-conditions) on Wiley Online Library for rules of use; OA articles are governed by the applicable Creative Commons License

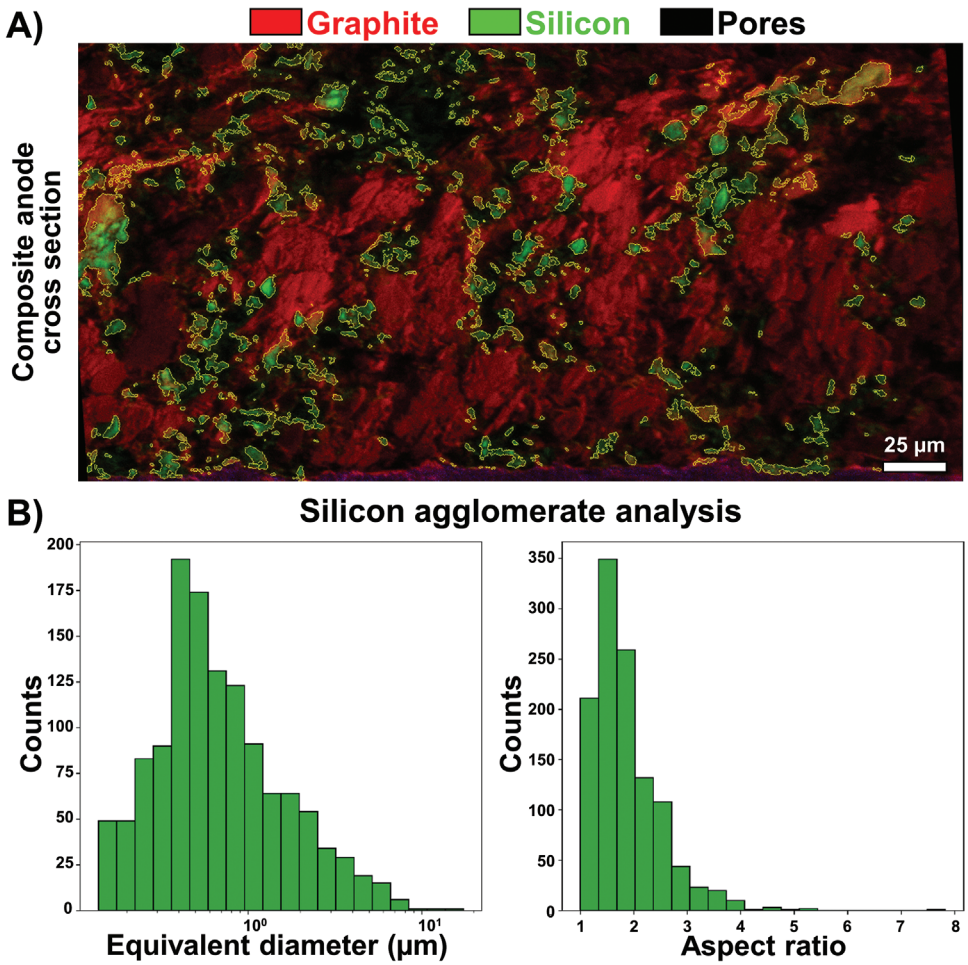

Figure 2. Example of identified silicon agglomerates in a non-calendered graphite-silicon composite anode. A) Cross-section of the electrode reporting the graphite + carbon (red) and silicon (green) regions identified by SIMS analysis. The borders of each silicon agglomerate are reported in yellow for visualization purposes. This image is obtained after a pre-processing step consisting of a series of digital filters applied to the original SIMS image (computational section) aiming to ease the separation of different particles/agglomerates. B) Si agglomerates size distribution (left) and aspect ratio (right). The equivalent diameter is the diameter of a circle of equivalent area compared to the identified particle/agglomerate, while the aspect ratio is defined as the ratio between its longer and shorter axis.

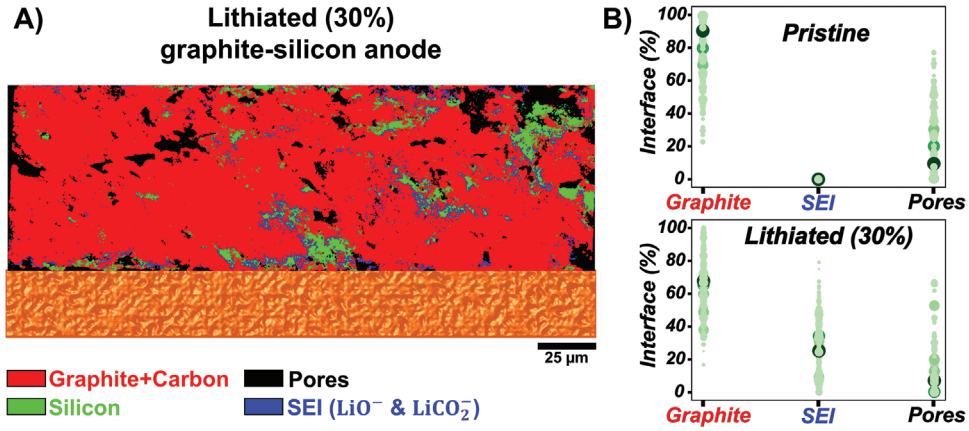

Figure 3. A) Example of segmented microstructure for a cycled (lithiated to 30% against lithium metal) graphite-silicon anode in which the spatial distribution of graphite + carbon additive (red), silicon (green), and SEI (blue) has been identified. The copper current collector on the bottom is drawn here for purely illustrative reasons. B) Percentage of interfaces of each silicon agglomerate covered either by graphite, SEI, or pores. The dots size and color are directly proportional to the equivalent diameter of the associated silicon agglomerate.

© 2023 The Authors. Advanced Materials Interfaces published by Wiley-VCH GmbH

21967350, 2023, 36, Downloaded from https://onlinelibrary.wiley.com/doi/10.1002/admi.202300640 by Justus Liebig Universitaet Giessen, Wiley Online Library on [02/10/2024]. See the Terms and Conditions (https://onlinelibrary.wiley.com/terms-and-conditions) on Wiley Online Library for rules of use; OA articles are governed by the applicable Creative Commons License

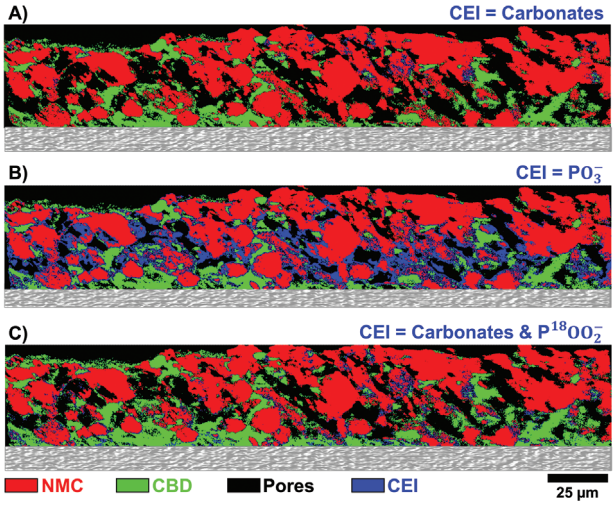

Figure 4. Example of segmented microstructure for the case of a cycled (500 cycles against a graphite anode at 1C) NMC electrode when using A) carbonates ($LiCO_3^-$ and CO_3^-), B) PO_3^-, or C) $P^{18}OO_2^-$ *plus* carbonates as reference SI signals to identify the spatial location of the CEI. CBD stands for carbon-binder domain. The aluminum current collector on the bottom of the electrode is drawn here for purely illustrative reasons.

CEI spatial distribution was found to be carbonates ($LiCO_3^-$ and CO_3^-) together with the $P^{18}OO_2^-$ signal (Figure 4C). Interestingly, as it can be noted in Figure 4, a phosphorous-rich CEI was found mainly on the current collector side (i.e., in a region subject to higher electronic current density), while a carbonate-rich CEI was found mainly on the separator side (i.e., in a region subject to higher ionic current density). This finding opens an interesting perspective for the methodology developed here, and in particular, the identification of which SEI/CEI/MIC regions are richer in given degradation products and how this is linked to the electrode microstructure, formulation, and cycling conditions.

2.2. Current Drawbacks and Limitations

Any analytical technique has its drawbacks and limitations, and the methodology developed in this work is no exception. Some of its drawbacks are intrinsic to the analytical technique used (ToF-SIMS), while others can be minimized with proper data analysis procedures or improved experimental setups.

1) Need for phase-specific SI. To map the phase and interphases spatial distribution by ToF-SIMS imaging it is necessary to identify phase-specific SIs. If this is not possible, two or more (inter)phases would become undistinguishable through this methodology. An example of this is the differentiation between conductive additive (carbon black) and graphite, which are both identified by carbon fragments (e.g., C^-, C_2^-, C_3^-, etc.). Similarly, we did not identify binder-specific SIs allowing to distinguish it from the carbon black. An interesting research direction for this could be the combination of positive and negative polarities measurements to increase the chances of identifying SI specific for each phase in the electrode. Furthermore, isotope labeling of individual components is an option to distinguish the origin of specific fragments, yet it requires additional steps during fabrication of electrodes.
2) Need for a compromise between SI ionization probability/lifetime and risks of artifacts. Especially for minor phases (like interphases) it is important to select SIs having high ionization probability, which allows detecting species of interest even at low concentrations. However, as illustrated for the case of PO_3^- (Figure 4B), SIs that have both particularly high ionization probability and lifetime may lead to artifacts, as the detection of signal originating from bulk particles underneath the electrode cross-section surface. In the case of cycled NMC-based cathodes, the combination of $P^{18}OO_2^-$, $LiCO_3^-$ and CO_3^- was found to be a good compromise between sensitivity and accuracy.
3) Need for suitable large areas cutting procedures. The quality of the SIMS-based microstructure depends on the quality of the cutting procedure. In the case of this work, the latter was performed through scissor cutting combined with FIB polishing (Experimental Section and Figure S1, Supporting Information). Clearly, this could be improved through devoted ion polishing systems.
4) Measurement time and cost. Acquiring SI images with the pixel resolution reported in this work in combination with a good mass resolution (delayed extraction mode) is time-consuming. The complete 2D analysis procedure (polishing and cleaning the electrode cross-section plus ToF-SIMS imaging) required ≈24 h per sample. Accordingly, for 3D SIMS analysis, measurements would have to be made at lower lateral resolution to ensure reasonable measurement times. If one wants to generate 3D images using ToF-SIMS (depth profiling), it must also be considered that the sputtered area should be at least two to three times larger than the analysis area, which further increases the analysis time. This currently hampers the direct sampling of 3D volumes (slice-by-slice, as for FIB-SEM). For this reason, we think that the combination with devoted ML procedures, today, is the best option for sampling large 3D microstructures through ToF-SIMS (next section).
5) In addition, ToF-SIMS is an expensive technique, meaning that not all research groups can have direct access to it, calling for collaboration between different research groups. It should be underlined, however, that this is characteristic not only for ToF-SIMS, and something similar could be said for the case of FIB-SEM as well as X-ray tomography.
6) Resolution. Despite ToF-SIMS being capable of achieving relatively high pixel resolution (50 nm for ideal flat surfaces, 100–150 nm for typical battery samples), it should be acknowledged that this technique falls short of the resolution achievable by other techniques such as (FIB-)SEM, which can reach resolutions as low as a few nm – but is less chemically specific.

2.3. ToF-SIMS and ML Combination to Unlock 3D Analyses

Experimental 3D electrode imaging requires combining high enough contrast to discriminate the different phases, high lateral resolutions to distinguish components of different sizes, and large sample volumes to obtain statistically relevant results. Adding to this already challenging list, the identification of

© 2023 The Authors. Advanced Materials Interfaces published by Wiley-VCH GmbH

21967350, 2023, 36, Downloaded from https://onlinelibrary.wiley.com/doi/10.1002/admi.202300640 by Justus Liebig Universitaet Giessen, Wiley Online Library on [02/10/2024]. See the Terms and Conditions (https://onlinelibrary.wiley.com/terms-and-conditions) on Wiley Online Library for rules of use; OA articles are governed by the applicable Creative Commons License

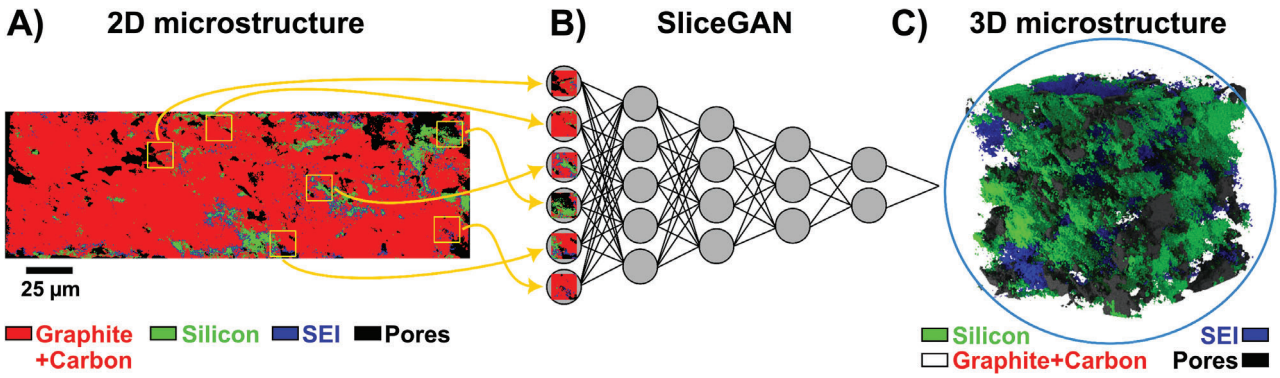

Figure 5. Schematics of the combination of A) SIMS-based 2D electrode microstructure and B) SliceGAN to generate C) statistically reconstructed 3D electrode microstructures accounting for the main phases and interphases spatial distribution. In the 3D microstructure (50 × 50 × 50 µm^3), the graphite + carbon phase is represented as transparent to allow a better look at its inner part. SliceGAN, as any GAN, is composed of two neural networks typically referred to as generator and discriminator, but it is schematically represented here with one neural network for simplicity.

interphases makes this challenge hardly possible at present. As we have shown in this work, high-resolution 2D ToF-SIMS imaging for electrode microstructure characterization provides sufficient contrast between different phases and interphases as well as high lateral resolution and large field of views. Nonetheless, obtaining all these characteristics currently causes the measurements to be particularly long (≈24 h in this study for only one image), making it unrealistic to go from 2D to 3D analyses through a slice-by-slice approach. This limitation can, however, be bypassed thanks to recent advancements in ML. In particular, Kench and Cooper recently published an algorithm (SliceGAN) based on generative adversarial networks (GANs) that can generate 3D electrode microstructures using, as input, large 2D microstructures.[28] This procedure was tested on several microstructures, demonstrating its statistical accuracy and great potential.[29]

In the context of this work, SliceGAN was applied for the first time to SI-based segmented 2D microstructures, with the final goal of training a model able to generate a statistical reconstruction of the 3D electrode microstructures accounting for the spatial distribution of the main phases *and* interphases, as schematically depicted in **Figure 5**. The goal of this analysis is to showcase that obtaining this kind of microstructure is now possible, opening possibilities for future research.

In short, SliceGAN picks, randomly, several sub-regions in the original 2D image (yellow squares in Figure 5) and trains two neural networks, typically referred to as generator and discriminator, using those sub-regions. The goal of the generator is to create microstructures that are statistically indistinguishable from the original ones, while the role of the discriminator is to distinguish between the original and artificial images. The training continues until it is not possible anymore to distinguish between the real and the artificial images. In other terms, during the training the generator learns how to reproduce the patterns found in the original 2D microstructure and, in addition to that, it is also able to translate this knowledge in a 3D space (Figure 5C).

To the best of our knowledge, the combination of the SIMS-based methodology developed in this work and SliceGAN is the only approach currently enabling the generation of realistic and large 3D microstructures containing information on the spatial distribution of the main phases *and* interphases. This kind of microstructure can then be embedded into devoted 3D electrochemical models to test different hypotheses on the role of the SEI/CEI spatial distribution on the electrochemical performance, which so far could be tested through stochastic approaches only.[33] It should be mentioned, however, that implementing these large and highly-resolved microstructures in a 3D electrochemical model could be challenging from a computational point of view due to convergence issues, which is a problem we have encountered with current COMSOL Multiphysics-based models. Adapting these electrochemical models for simulating the 3D electrodes generated in this study was out of the scope of this work, but we are confident that other researchers can use our result as a starting point to update their 3D electrochemical models to account for the SEI or CEI spatial distribution.

3. Conclusions

This article presents a novel analytical methodology that enables the acquisition of large battery electrode microstructures providing information on the spatial distribution of both main phases and interphases. To the best of our knowledge, to date no other approach enables this, making the methodology presented here a step forward in the context of battery electrode microstructure characterization. This is relevant because both the electrode microstructure and interphases (SEI, CEI, or MCI) are widely recognized to be key for battery electrochemical performance, safety, cycle, and calendar life.

The methodology presented in this work is based on ToF-SIMS imaging and was applied to characterize the 2D electrode microstructures (cross-section) of state-of-the-art cathodes (NMC-based) and anodes (graphite-silicon-based). It has been proven that the spatial distribution of the SEI (using LiO^- and $LiCO_2^-$ as reference SIs), CEI (using $LiCO_3^-$, CO_3^-, and $P^{18}OO_2^-$ as reference SIs), active materials (NMC, graphite, and silicon), and additives (CBD for the case of the cathode) can be detected through this methodology. Combining all this information allows for obtaining a representative (in our case 250 × electrode thickness µm^2) 2D electrode microstructure accounting for the spatial distribution of the main phases *and* interphases (Figures 3 and 4).

Combining high-resolution SIMS imaging and a devoted ML procedure, namely SliceGAN, enables to learn from the patterns

© 2023 The Authors. Advanced Materials Interfaces published by Wiley-VCH GmbH

21967350, 2023, 36, Downloaded from https://onlinelibrary.wiley.com/doi/10.1002/admi.202300640 by Justus Liebig Universitaet Giessen, Wiley Online Library on [02/10/2024]. See the Terms and Conditions (https://onlinelibrary.wiley.com/terms-and-conditions) on Wiley Online Library for rules of use; OA articles are governed by the applicable Creative Commons License

found in the original SIMS-based 2D microstructure and reconstruct statistically representative 3D electrode microstructure (Figure 5). This allows generating statistically representative 3D electrode microstructures accounting for the primary electrode microstructure and the interphases spatial distribution. Such advancements hold significant value for the 3D battery modeling community, offering new avenues for research and analysis. These microstructures could indeed be used to test different hypotheses on the role of the SEI/CEI, and its spatial distribution, on the electrochemical performance, which so far has been tested only through stochastic approaches. The 2D SIMS-based microstructures obtained in this work are also published with this article in a format suited for SliceGAN, for possibly interested researchers to use them as a starting point for their electrochemical models.

In terms of perspective, we are convinced that ToF-SIMS in general, and this methodology in particular, holds great benefits for battery electrode microstructure characterization and we invite the battery community to further explore its potential in the quest for correlations between electrodes microstructure, interfaces, interphases, and performance.

4. Experimental Section

Electrodes Manufacturing and Cycling: Artificial graphite, conductive graphite (TIMREX SFG6L), and carbon black (C-NERGY super C65) were provided by IMERYS. SiO_x (AS2D) was provided by ShanShan Tech. $LiNi_{0.6}Mn_{0.2}Co_{0.2}O_2$ (NMC) and *N*-methyl-2-pyrrolidone (NMP) were provided by BASF. Polyvinylidene fluoride (PVdF) Solef 5130 was provided by SAFT. Polyacrylic acid (PAA – 240 kg mol^{-1}) was provided by Acros Organics. Carboxymethyl cellulose (CMC) 2000PA was provided by DOW Chemical. Styrene-butadiene- rubber (SBR) BM-451B was provided by Zeon Europe.

The anode formulation is 70 wt.% of artificial graphite, 20 wt.% SiO_x, 2 wt.% C65, 4 wt.% PAA, 2 wt.% CMC, and 2 wt.% SBR. The solid components (artificial graphite, SiO_x, C65, and CMC) were mixed in a Turbula 3D Mixer (Willy A. Bachofen AG) for 15 min at 49 rpm. Then the powders are added to the solution (in deionized water) containing PAA and mixed in a Dispermat CA60 (VMA-Getzmann GmbH) at 15 °C following a two steps procedure (PAA+ LiOH to neutralize the solution, 45 min at 9 m s^{-1} tangential speed). Finally, the SBR solution was added and mixed at low shear-rate to avoid damages (15 min at 3 m s^{-1} tangential speed) while degassing. The final slurry solid content was equal to 40 wt.%. The cathode solid components (95.5 wt.% NMC, 1.5 wt.% C65, 0.75 wt.% conductive graphite, 2.25 wt.% PVdF) were dry mixed for 13 min at 480 and 100 rpm. Afterward, solvent (NMP) was added in two steps (first up to a SC of 83 wt.% and then up to 75 wt.%) and mixed for 30 min at 600 and 100 rpm. Both dry and wet mixing were performed in a PMH10 planetary mixer (NETZSCH GmbH und Co. Holding AG).

Anode and cathode were coated and dried using a LabCo (Kroenert GmbH & Co. KG) device with an oven composed of three segments (each one 2 m long) whose temperature can be controlled separately. The anode slurry was coated on a copper current collector (10 µm thick) at a speed of 1.5 m s^{-1} and at 60 °C in all the three ovens. The cathode slurry was coated on an aluminum current collector (20 µm thick) at a speed of 2 m^{-1}s and at 80, 100, and 120 °C in the first, second, and third ovens, respectively.

Anode and cathode were calendered using a FKL 400 (SAUERESSIG GmbH und Co. KG) device until reaching an electrode density of 1.3 and 3 g cm^{-3}, respectively.

Prelithiation (30%) was performed in half-cell (Gri-SiO_x versus Li-metal) configuration in a pouch cell format (single layer, 5.5 × 5.5 cm^2). The electrode was then washed in EMC, dried under argon, and finally cut in circular discs for further analysis. The electrolyte used for the prelithiation step was the same as for full-cell cycling (see below).

The coated/prelithiated electrodes were cut in circular 18 mm diameter disks. The average anode and cathode loadings were 8 and 16 mg cm^{-2}, respectively. The thickness (including the current collector), density, and porosity after calendering for the anode and cathode were ca. 72 µm, 1.3 g cm^{-3}, 40% and 74 µm, 3 g cm^{-3}, 30%, respectively. The cell used was s PAT-Cell from EL-CELL. The separator used is FS-5P 220 µm double layer separator (Freudenberg Viledon FS 2226 E + Lydall Solupor 5P09B) with 100 µL electrolyte (LP57 (1 mol $LiPF_6$ in EC:EMC (3:7, by wt.) + 2 wt.% VC + 10 wt.% FEC. Supplier: E-Lyte Innovations GmbH).

Full-cell cycling was performed at 1C (1C = 170 mAh g_{NMC}^{-1}) between 2.9 and 4.2 V, with a formation step consisting of 1 cycle at 0.1 C and 2 cycles at 0.2 C. The same current was used for both charge and discharge (symmetric protocol).

After cycling, the cells were opened inside a glovebox ($p(O_2)/p$ < 0.1 ppm and $p(H_2O)/p$ < 0.1 ppm), the electrodes were carefully separated and washed in battery grade EMC, then dried under vacuum and prepared for transport (more details below).

Sample Shipping and Transfer: All the electrodes were wrapped in cleaned copper foil and placed in small snap-on lid jars, which were sealed in two pouch bags for shipping, the inner one under vacuum and the external one filled with argon. This procedure should prevent the electrodes from being exposed to air even if the vacuum (first pouch) is broken during transport. The electrodes were stored in an argon-filled glovebox ($p(O_2)/p$ < 0.1 ppm and $p(H_2O)/p$ < 0.1 ppm) as soon as received. The electrodes were first cut with a scissor to expose their cross-section in the Ar-filled glovebox (polishing performed at the SIMS, as discussed below) and then placed in a sample holder exposing their cross-section to the primary gun, the analyzer, and the FIB gun (Figure S1, Supporting Information). The samples were transferred from the glovebox to the ToF-SIMS using the Leica EM VCT500 (Leica Microsystems GmbH) transfer system.

Secondary Ion Mass Spectrometry (SIMS) Measurements: All the measurements were performed with a ToF-SIMS 5-100 system (IONTOF GmbH). The system was equipped with a 25 keV Bi cluster primary ion gun for analysis and a dual-source column, which enables depth profiling by using either O_2^+ or Cs^+ (up to 2 keV). In addition, the instrument was equipped with a focused ion beam (FIB) based on monatomic gallium (30 keV), which was used to polish the electrode cross-sections.

Polishing of electrode cross-sections was done through FIB, with a FIB current of ≈30 nA (100% duty cycle). First, a 700 µm aperture was used with a dwell time of 200 ms per pixel (FoV: 500 × 150 $µm^2$, 256 × 256 pixels). Afterward, for fine polishing, dwell time was reduced to 70 ms per pixel, and raster size was increased to 512 × 512 pixels. Finally, the cross-sections were cleaned by applying the primary ion gun in direct current (DC) mode for 30 min.

High-resolution imaging analyses of polished cross-sections were performed in negative ion mode using Bi_3^+ (25 keV) as primary ion species for analysis with primary ion currents of ≈0.35–0.40 pA. Cycle time was set to 60 µs. Analysis was done in delayed extraction mode with delay times between 0.030 and 0.050 µs. Surface areas of 250 × electrode thickness $µm^2$ were rasterized in random mode with 2048 × 2048 pixels, 5 shots per pixel, and 1 frame. Measurements were stopped after 150–250 scans. During all measurements, charge compensation was done with a low-energy electron flood gun. Mass resolution $m/\Delta m$ (mass divided by the full width at half maximum) was for all measurements >5000 at m/z 60.00 (C_5^-).

The first evaluation of ToF-SIMS data was done with the software SurfaceLab 7.3 (IONTOF GmbH).

Computational Section: The code to perform the SIMS-based image recombination and segmentation was built in Python (Jupyter Notebook) and it is published with this article (https://github.com/teolombardo/Electrode-Microstructure-and-Interphases-Characterization-by-Combining-ToF-SIMS-and-Machine-Learning.git), together with a documentation file and an example (cycled NMC). The original images were pre-processed using digital filters, and the exact procedure was slightly adapted as a function of the experimental image obtained (typically using a median filter to remove salt and pepper

© 2023 The Authors. Advanced Materials Interfaces published by Wiley-VCH GmbH

21967350, 2023, 36, Downloaded from https://onlinelibrary.wiley.com/doi/10.1002/admi.202300640 by Justus Liebig Universitaet Giessen, Wiley Online Library on [02/10/2024]. See the Terms and Conditions (https://onlinelibrary.wiley.com/terms-and-conditions) on Wiley Online Library for rules of use; OA articles are governed by the applicable Creative Commons License

type artifacts and a non-local mean filter to improve overall image quality). Running this code took a few minutes using an Intel(R) Core(TM) i5-10500 CPU @ 3.10 GHz (16 Gb of RAM). The single particle/agglomerate identification was performed through a water-shed-based algorithm (included in the published code). SliceGAN[34] was run on the CPU of an 11th Gen Intel(R) Core(TM) i7-11700 @ 2.50 GHz (96 Gb of RAM) and took ca. 72 h for the training (and, after the training, a few minutes to generate a 3D electrode microstructure of 50 × 50 × 50 μm^3). However, it should be underlined that, if using GPU instead of CPU, the training time would have drastically decreased (typically < 2 h), as shown by the original developers of SliceGAN.

Supporting Information

Supporting Information is available from the Wiley Online Library or from the author.

Acknowledgements

T.L. and C.K. contributed equally to this work. T.L, C.K., J.S., M.R., and J.J. acknowledge the support by the Federal Ministry of Education and Research (BMBF, Bundesministerium für Bildung und Forschung) within the ProGraL project (Grant no. 03XP0427). J.J. also acknowledges the support by Federal Ministry of Education and Research (BMBF, Bundesministerium für Bildung und Forschung) within the BMBF Cluster of Competence FESTBATT (Grant no. 03XP0433D). T.L. acknowledges Chao Liu from the Laboratoire de Réactivité et Chimie des Solides (LRCS) in Amiens (France), under the supervision of Prof. Alejandro A. Franco from the LRCS in Amiens (France), for trying to implement in a 3D electrochemical model (based on COMSOL Multiphysics) the NMC-based 3D electrode microstructure generated during this study (tests failed due to convergence issues). T.L. acknowledges Steven Kench from the Imperial College of London (UK) for his support on the utilization of SliceGAN. The authors acknowledge Hans Fenske (Institute for Particle Technology Technische Universität Braunschweig, Germany) for the manufacturing and cycling of the graphite-silicon and NMC-based electrodes analyzed in this work.

Open access funding enabled and organized by Projekt DEAL.

Conflict of Interest

The authors declare no conflict of interest.

Data Availability Statement

Raw data sets of ToF-SIMS measurements are published under http://dx.doi.org/10.22029/jlupub-17832.

Keywords

cathode-electrolyte interphase, electrode microstructures, lithium-ion batteries, machine learning, time-of-flight secondary ion mass spectrometry (ToF-SIMS)

Received: July 28, 2023
Revised: September 4, 2023
Published online: September 25, 2023

[1] H. Xu, J. Zhu, D. P. Finegan, H. Zhao, X. Lu, W. Li, N. Hoffman, A. Bertei, P. Shearing, M. Z. Bazant, *Adv. Energy Mater.* **2021**, *11*, 2003908.
[2] W. B. Hawley, J. Li, *J. Energy Storage* **2019**, *25*, 00862.
[3] X. Lu, A. Bertei, D. P. Finegan, C. Tan, S. R. Daemi, J. S. Weaving, K. B. O'regan, T. M. M. Heenan, G. Hinds, E. Kendrick, D. J. L. Brett, P. R. Shearing, *Nat. Commun.* **2020**, *11*, 2079.
[4] H. Nakajima, T. Kitahara, Y. Higashinaka, Y. Nagata, *ECS Trans.* **2015**, *64*, 87.
[5] B. Ludwig, Z. Zheng, W. Shou, Y. Wang, H. Pan, *Sci. Rep.* **2016**, *6*, 23150.
[6] J. Kumberg, M. Müller, R. Diehm, S. Spiegel, C. Wachsmann, W. Bauer, P. Scharfer, W. Schabel, *Energy Technol.* **2019**, *7*, 1900722.
[7] H. Hagiwara, W. J. Suszynski, L. F. Francis, *J. Coat. Technol. Res.* **2014**, *11*, 11.
[8] R. Morasch, J. Landesfeind, B. Suthar, H. A. Gasteiger, *J. Electrochem. Soc.* **2018**, *165*, A3459.
[9] S. Jaiser, M. Müller, M. Baunach, W. Bauer, P. Scharfer, W. Schabel, *J. Power Sources* **2016**, *318*, 210.
[10] C. Meyer, H. Bockholt, W. Haselrieder, A. Kwade, *J. Mater. Process. Technol.* **2017**, *249*, 172.
[11] E. N. Primo, M. Chouchane, M. Touzin, P. Vazquez, A. A. Franco, *J. Power Sources* **2021**, *488*, 229361.
[12] A. N. Mistry, K. Smith, P. P. Mukherjee, *ACS Appl. Mater. Interfaces* **2018**, *10*, 6317.
[13] A. Bielefeld, D. A. Weber, J. Janek, *J. Phys. Chem. C* **2019**, *123*, 1626.
[14] A. Shodiev, E. N. Primo, M. Chouchane, T. Lombardo, A. C. Ngandjong, A. Rucci, A. A. Franco, *J. Power Sources* **2020**, *454*, 227871.
[15] M. Chouchane, A. Rucci, T. Lombardo, A. C. Ngandjong, A. A. Franco, *J. Power Sources* **2019**, *44*, 227285.
[16] T. Lombardo, F. Caro, A. C. Ngandjong, J.-B. Hoock, M. Duquesnoy, J. C. Delepine, A. Ponchelet, S. Doison, A. A. Franco, *Batter. Supercaps* **2022**, *5*, 202100324.
[17] L. Zielke, T. Hutzenlaub, D. R. Wheeler, C.-W. Chao, I. Manke, A. Hilger, N. Paust, R. Zengerle, S. Thiele, *Adv. Energy Mater.* **2015**, *5*, 1401612.
[18] L. Almar, J. Joos, A. Weber, E. Ivers-Tiffée, *J. Power Sources* **2019**, *427*, 1.
[19] J. Joos, A. Buchele, A. Schmidt, A. Weber, E. Ivers-Tiffée, *Energy Technol.* **2021**, *9*, 2000891.
[20] M. Ebner, D.-W. Chung, R. E. García, V. Wood, *Adv. Energy Mater.* **2014**, *4*, 1301278.
[21] S. Müller, J. Eller, M. Ebner, C. Burns, J. Dahn, V. Wood, *J. Electrochem. Soc.* **2018**, *165*, A339.
[22] B. L. Trembacki, D. R. Noble, V. E. Brunini, M. E. Ferraro, S. A. Roberts, *J. Electrochem. Soc.* **2017**, *164*, E3613.
[23] B. L. Trembacki, A. N. Mistry, D. R. Noble, M. E. Ferraro, P. P. Mukherjee, S. A. Roberts, *J. Electrochem. Soc.* **2018**, *165*, E725.
[24] M. E. Ferraro, B. L. Trembacki, V. E. Brunini, D. R. Noble, S. A. Roberts, *J. Electrochem. Soc.* **2020**, *167*, 013543.
[25] T.-T. u. Nguyen, J. Villanova, Z. Su, R. Tucoulou, B. Fleutot, B. Delobel, C. Delacourt, A. Demortière, *Adv. Energy Mater.* **2021**, *11*, 2003529.
[26] V. Wood, *Nat. Rev. Mater.* **2018**, *3*, 293.
[27] M. Winter, B. Barnett, K. Xu, *Chem. Rev.* **2018**, *118*, 11433.
[28] S. Kench, S. J. Cooper, *Nat. Mach. Intell.* **2021**, *3*, 299.
[29] S. Kench, I. Squires, A. Dahari, S. J. Cooper, *Sci Data* **2022**, *9*, 645.
[30] T. Lombardo, F. Walther, C. Kern, Y. Moryson, T. Weintraut, A. Henss, M. Rohnke, *J. Vac. Sci. Technol. A* **2023**, *41*, 053207.
[31] E. Peled, S. Menkin, *J. Electrochem. Soc.* **2017**, *164*, A1703.
[32] A. Bhowmik, I. E. Castelli, J. M. Garcia-Lastra, P. B. Jørgensen, O. Winther, T. Vegge, *Energy Stor. Mater.* **2019**, *21*, 446.
[33] M. Chouchane, O. Arcelus, A. A. Franco, *Batter. Suppercaps* **2021**, *4*, 1457.
[34] https://github.comstke9/SliceGAN, (accessed: October 2022).

© 2023 The Authors. Advanced Materials Interfaces published by Wiley-VCH GmbH

21967350, 2023, 36, Downloaded from https://onlinelibrary.wiley.com/doi/10.1002/admi.202300640 by Justus Liebig Universitaet Giessen, Wiley Online Library on [02/10/2024]. See the Terms and Conditions (https://onlinelibrary.wiley.com/terms-and-conditions) on Wiley Online Library for rules of use; OA articles are governed by the applicable Creative Commons License